to $\mathbf{n}$ when $\nabla \cdot \mathbf{n}$ is positive. A nematic drop with $Q = 1$ has nonvanishing positive splay everywhere. This splay acts as an external field that establishes minimum energy positions for droplet dipoles and thereby arrests Brownian motion. The minimum energy position of a single droplet is at the center of a nematic drop. A second droplet moves to maximum splay at the center with $\mathbf{p}$ pointing toward the center along negative $\mathbf{n}$ in accord with observations. Subsequent droplets form chains. In contrast, in the parallel geometry there is no splay localizing particles; as a result, the particles and chains undergo Brownian motion, which leads to interchain coagulation.

Finally, one of the most important features of these novel colloidal interactions is their dependence on the anchoring of the nematic at the interface. For example, the behavior of the colloidal droplets in the multiple emulsions is completely altered if the nematic is forced to align parallel to the surface of the large droplets rather than perpendicular. In the passage from homeotropic to tangential alignment, the topological charge interior to a nematic drop is changed from 1 to 0, and point defects called boojums (*2*) develop on its surface. Splay is a maximum in the vicinity of these boojums, and thus we would expect the colloidal droplets to congregate at these defects. We can achieve tangential boundary conditions at the surface of the nematic drops, but not at the surfaces of interior colloidal water droplets, by adding a small amount of glycerol to the continuous water phase. As expected, the colloidal droplets do indeed migrate to the boojums. Similarly, in our theory, both the chaining and the defect-mediated repulsion are a consequence of the dipolar defect configuration produced by a droplet with homeotropic boundary conditions. Droplets with tangential boundary conditions create neither a radial nor a companion hyperbolic hedgehog and should, therefore, exhibit completely different structures. To test this, we added polyvinyl alcohol to the water droplets to change boundary conditions from homeotropic to tangential. The tendency to form chains was greatly reduced; moreover, the droplets were no longer separated by large distances when they approached one another, reflecting the absence of the hedgehog defects.

The new class of colloidal interactions discussed in this paper is not restricted to thermotropic nematic LC but should be present whenever the host fluid is anisotropic. Interesting effects can be expected as the delicate balance among the magnitude of the elastic constant, the particle size, and the anchoring energies is adjusted. For example, this class of interactions should also be present for solutions of anisotropic micelles (*10*), rigid-rod polymers, and even biological systems such as actin or viruses. Moreover, the ability to controllably obtain both attractive and repulsive interactions offers an opportunity to develop novel routes to colloid stabilization and structure, as well as to create new materials with potentially useful applications. The theoretical picture presented here provides the framework for understanding all of these phenomena.

REFERENCES AND NOTES

1. W. B. Russel, D. A. Saville, W. R. Schowalter, *Colloidal Dispersions* (Cambridge Univ. Press, Cambridge, 1989).
2. M. V. Kurik and O. D. Lavrentovich, *Usp. Fiz. Nauk*, **154**, 381 (1988) [*Sov. Phys. Usp.* **31**, 196 (1988)]; N. D. Mermin, *Rev. Mod. Phys.* **51**, 591 (1979).
3. P. G. de Gennes and J. Prost, *The Physics of Liquid Crystals* (Clarendon, Oxford, ed. 2, 1993); S. Chandrasekhar, *Liquid Crystals* (Cambridge Univ. Press, Cambridge, 1992).
4. E. M. Terentjev, *Phys. Rev. E* **51**, 1330 (1995); O. V. Kuksenpk, R. W. Ruhwandl, S. V. Shiyanovskii, E. M. Terentjev, *ibid.* **54**, 5198 (1996).
5. S. Ramaswamy, R. Nityananda, V. A. Garhunathan, J. Prost, *Mol. Cryst. Liq. Cryst.* **288**, 175 (1996).
6. R. B. Meyer, *ibid.* **16**, 355 (1972).
7. S. Ostlund, *Phys. Rev. B* **24**, 485 (1981).
8. R. B. Meyer, *Phys. Rev. Lett.* **22**, 918 (1969).
9. A. P. Gast and C. F. Zukoski, *Adv. Colloid Interface Sci.* **30**, 153 (1989).
10. P. Poulin, V. A. Raghunathan, P. Richetti, D. Roux, *J. Phys. II France* **4**, 1557 (1994).

11. We are grateful to A. Yodh for helpful discussions and a careful reading of the manuscript and to F. Macera for help with the figures. Supported primarily by the Materials Research Science and Engineering Center Program of NSF under award number DMR96-32598.

30 September 1996; accepted 7 February 1997

Direct Radiometric Observations of the Water Vapor Greenhouse Effect Over the Equatorial Pacific Ocean

Francisco P. J. Valero,* William D. Collins, Peter Pilewskie, Anthony Bucholtz, Piotr J. Flatau

Airborne radiometric measurements were used to determine tropospheric profiles of the clear sky greenhouse effect. At sea surface temperatures (SSTs) larger than 300 kelvin, the clear sky water vapor greenhouse effect was found to increase with SST at a rate of 13 to 15 watts per square meter per kelvin. Satellite measurements of infrared radiances and SSTs indicate that almost 52 percent of the tropical oceans between 20°N and 20°S are affected during all seasons. Current general circulation models suggest that the increase in the clear sky water vapor greenhouse effect with SST may have climatic effects on a planetary scale.

Recent studies (*1*) have demonstrated that atmospheric general circulation models, when forced only with measured SSTs (in particular, tropical Pacific SSTs), can reproduce the changes in global tropospheric temperatures that have been observed during the last several decades (*2, 3*). Earlier results (*4–6*) also pointed to the existence of a relation between variations in the tropical Pacific SSTs and global tropospheric temperatures. In this context, the clear sky water vapor greenhouse effect is key to the understanding of climate change, including global warming (*7*). The greenhouse effect can be defined as (*8–10*)

$$G_a = \sigma(\mathrm{SST})^4 - F^+ \qquad (1)$$

F. P. J. Valero, W. D. Collins, A. Bucholtz, P. J. Flatau, Atmospheric Research Laboratory, Center for Atmospheric Sciences, Scripps Institution of Oceanography, University of California, San Diego, 9500 Gilman Drive, La Jolla, CA 92093–0242, USA.
P. Pilewskie, NASA, Ames Research Center, Moffett Field, CA 94035, USA.
*To whom correspondence should be addressed.

According to the Stefan Boltzmann law, $\sigma(\mathrm{SST})^4$ is the infrared black body emission by the surface at temperature SST, $\sigma = 5.67 \times 10^{-8}$ W m^{-2} K^{-4} is the Stefan Boltzmann constant, and F^+ is the outgoing infrared radiation flux at the top of the atmosphere.

Satellite studies (*8–10*) have found that for clear skies and SSTs above 298 K, the spatial variation of G_a with SST, $dG_a/d(\mathrm{SST})$, exceeds the rate of increase of sea surface emission, $d\sigma(\mathrm{SST})^4/d(\mathrm{SST}) = 4\sigma(\mathrm{SST})^3$. For a tropical SST of 300 K, $4\sigma(\mathrm{SST})^3 \approx 6.1$ W m^{-2} K^{-1}. This effect, termed the "super greenhouse effect" (*11*), occurs in both hemispheres during all seasons. It is also observed for interannual variations of G_a with SST during the El Niño in the tropical Pacific (*12*). Observations in the tropical Atlantic ocean (*11*) show that the clear sky downwelling infrared flux incident on the surface (F_a^-) also increases faster than the surface emission with increasing SST. The net result is fur-

ther warming of the surface, which in turn induces additional heating of the atmospheric column above. The increase of G_a and F_a^- with SST is linked to the augmentation in column water vapor content with SST and lapse rate (*8*). The super greenhouse effect is thus defined as (*8*, *10*)

$$dG_a/d(SST) > d[\sigma(SST)^4]/d(SST) \quad (2)$$

at the top of the atmosphere, and as

$$dF_a^-/d(SST) > d[\sigma(SST)^4]/d(SST) \quad (3)$$

at the surface.

Here we report direct observations of the tropospheric super greenhouse effect and investigate the processes by which the clear sky water vapor greenhouse effect heats the atmospheric column and the ocean surface. In particular, we focus on the following questions. How extensive is the area where $dG_a/d(SST) > 4\sigma(SST)^3$? Is it a long-term effect, or does it occur only during limited times? How much energy is trapped? Is the radiative energy transported to the extra tropics by the atmosphere, or does it contribute locally to the heating of the sea surface and consequently to climate variability on a planetary scale?

We used satellite radiances from the Earth Radiation Budget Experiment and SST measurements (*8*, *10*) to determine the areal extent and regions of the tropical oceans where the temporal rate of increase in G_a exceeds the rate for the surface emission (Fig. 1). We found that during all seasons in the period 1985 to 1989, the super greenhouse effect occurred over 52% of the tropical sea surface between 20°N and 20°S, in the Atlantic, Indian, and Pacific oceans.

In situ radiometric observations of infrared irradiances and radiances were made with multiple aircraft flying in coordinated, simultaneous tracks several thousand kilometers long during the Central Equatorial Pacific Experiment (Fig. 1). The NASA ER-2, the Aeromet Learjet, and the National Oceanic and Atmospheric Administration (NOAA) P-3 aircraft were flown at altitudes of 20 km, 11 km, and in the lower troposphere, respectively. Atmospheric irradiances from the lower troposphere to the tropopause were measured covering the full range of SSTs between 165°E and 170°W longitudes at 2°S latitude. More than 4×10^6 km^2 were sampled during the period from 7 March to 4 April 1993, for a total of more than 100 hours of flight for each aircraft.

Two identical radiation measuring systems (RAMS), which are multiple instrument arrays, were deployed on the ER-2 and Learjet airborne platforms to profile the mid- and upper troposphere up to the tropopause. The RAMS upper and mid-troposphere radiative measurements and instruments pertinent to this super greenhouse effect study are as follows (*13*, *14*): (i) spectral broadband (4 to 40 μm) infrared

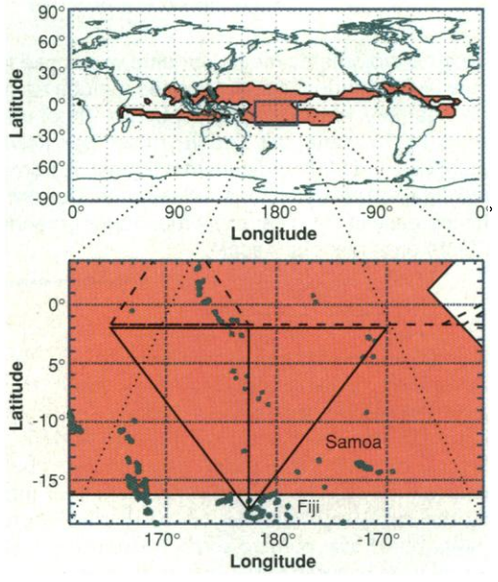

Fig. 1. Map of the clear sky water vapor greenhouse effect for each 2.5° (latitude) by 2.5° (longitude) region where the monthly mean SST exceeded 298 K for all months during 1985 to 1989. The values $dG_a/d(SST)$ and $d\sigma(SST)^4/d(SST)$ were calculated by least squares regression of the monthly mean G_a, calculated with infrared radiances from the Earth Radiation Budget Experiment, and $\sigma(SST)^4$ against SST. The errors in SST and F^+_{clear} used in the regression are 0.5 K and 5 W m^{-2}, respectively (*12*, *15*). Regions where the difference between $dG_a/d(SST)$ and $d\sigma(SST)^4/d(SST)$ is more than twice the root-mean-square error (indicating super greenhouse effect) are colored. Flights were made in the enlarged region where representative flight tracks of the ER-2 and Learjet (solid lines) and P-3 (dashed lines) are indicated.

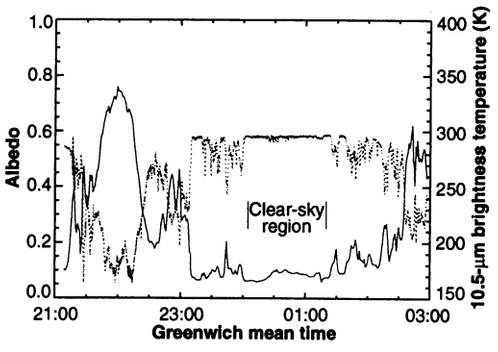

Fig. 2. RAMS 10.5-μm (nadir viewing) brightness temperature (dashed line) and broadband solar albedo (solid line) measured from the ER-2 during the flight on 15 March 1993 over the 2°S latitude belt between 180°E and 170°W. An example of data classified as clear sky is indicated.

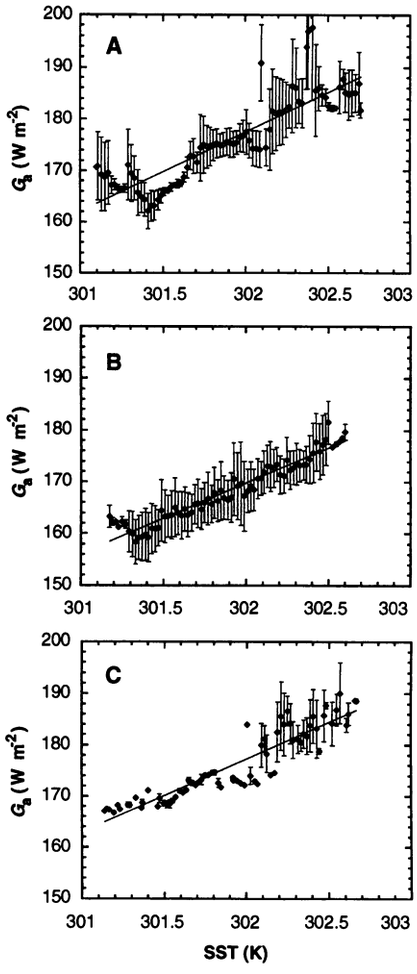

Fig. 3. Clear sky greenhouse effect versus SST as observed from the ER-2 (69-mbar altitude) and Learjet (191-mbar altitude) aircraft. The plots show data from six flights. Each individual flight covered the full range of SSTs along the 2°S track (Fig. 1). Data points represent the average of the clear-sky data points in 0.02 K SST intervals. The standard deviations are indicated by bars. The figures show regressions with data from (**A**) the IRBBR on the ER-2, correlation factor (R) = 0.871; (**B**) the IRBBR on the Learjet, R = 0.964; and (**C**) the NFOV radiometer on the ER-2, R = 0.921.

upwelling irradiance was measured with an infrared broadband radiometer (IRBBR); (ii) spectral broadband (0.3 to 4.0 μm) upwelling and downwelling solar irradiances were measured with a solar broadband radiometer; (iii) narrow spectral bandwidth (~1 μm, centered at 10.5 μm) upwelling radiance and brightness temperature were measured with a narrow field of view infrared radiometer (NFOV); and (iv) spectral broadband (4 to 40 μm) upwelling radiance was also measured with an NFOV.

The radiometric precision of the RAMS is better than 1%. The absolute infrared accuracy depends on the calibrating black bodies and is estimated to be about 1 to 2%. The calibration of the solar radiometers is accurate to 1 to 2% as determined by comparison with a National Institute of Standards radiation reference.

The P-3 aircraft, dedicated to measurements in the lower and mid-troposphere, was equipped with broadband infrared and solar flux radiometers different from those in the other two aircraft. A comparison of the Learjet and P-3 infrared measurements suggests a discrepancy of about 5% of the upwelling irradiance at 400 mbar.

SSTs used in this study were obtained from a combined analysis of satellite and in situ data from NOAA and the National Meteorological Center (*15*). The SSTs are accurate to 0.3 K as determined by comparison with ship measurements during the period of the observations. Relative SSTs are precise to less than 0.1 K. SSTs in the experimental region ranged from about 300 to 303 K.

Using concurrent brightness temperature data, solar broadband albedo measurements, lidar data (*16*), spectral modis airborne simulator (MAS) (*17*), and photographic images (wide angle camera) acquired from the ER-2 aircraft, we made a thorough assessment to distinguish between clear and cloudy conditions and to ensure that the observed greenhouse effect was not due to cirrus radiative absorption as a result of classification error. Similar classification schemes have been used in satellite studies (*18*). These cloud screening criteria are based on a comparison of infrared brightness temperatures (IRBTs) from the NFOV spectral radiometer and the MAS imager with the cloud detection lidar on the ER-2. The criteria to define clear sky and to select data used to derive G_a were a hemispherical shortwave albedo <0.1 (characteristic of clear skies), an NFOV IRBT and average MAS IRBT ≥290 K, and more than 90% of the MAS pixel IRBTs ≥290 K (Fig. 2). The cloud detection lidar was used to identify the radiative characteristics of cloud-free pixels in the MAS images. A total of 99.7% of clear sky nadir pixels had IRBTs ≥290 K; less than 0.4% of optically thick clouds had IRBTs ≥290 K. The MAS images coincident with the RAMS data were then scanned to eliminate cloud-contaminated measurements. The data show that some low-altitude broken clouds somewhat affect the albedo but do not affect the infrared fluxes significantly because their temperature is close to the surface temperature. In the case of the P-3 aircraft, an additional requirement was imposed to select valid data points; namely, the airplane must not have changed altitude by more than 100 m during the previous 9 min. This requirement ensured that the P-3 radiometers had equilibrated with the ambient temperature.

With the criteria described above, the data were segregated into clear sky and cloud-covered regimes. Clear sky G_a values derived from irradiances measured with the IRBBRs were averaged at each SST for each flight altitude. SST values were linearly interpolated between measured surface temperatures. The clear sky values of G_a at altitudes of 69 and 191 mbar were then plotted against SST (Fig. 3). A least squares linear regression fit (a good approximation over narrow SST ranges) to the clear sky data points (solid lines in Fig. 3, A and B) gives $G_a = [146.9 + 15.3(SST - 300)]$ W m^{-2} at 69-mbar altitude (ER-2) and $G_a = [142.7 + 13.5(SST - 300)]$ W m^{-2} at 191-mbar altitude (Learjet).

The relation of G_a to SST was also derived from the broadband upwelling (4 to 40 μm) radiances measured with the NFOV nadir-pointing radiometer on the ER-2. Clear sky scenes were identified with the nadir-pointing cloud lidar that has a field of view larger than the NFOV. This procedure guarantees that within the limit of detection of the lidar the clear sky NFOV data are free of the effect of thin cirrus clouds. The irradiances were derived from the radiances by multiplying by a constant factor of 0.893π, which was experimentally derived by comparing simultaneous radiance and irradiance measurements from the ER-2 aircraft. A regression of G_a computed from the NFOV radiances with SST (Fig. 3C) gives $G_a = [148.6 + 14.2(SST - 300)]$ W m^{-2} at 69-mbar altitude. The excellent agreement between the G_a's derived from NFOV radiances and IRBBR irradiances indicates that the observed variation in greenhouse effect is not related to cirrus cloud contamination. The aircraft-measured $dG_a/d(SST)$ values are more than double the rate of

Table 1. Comparison of satellite and aircraft determinations of $dG_a/d(SST)$. The difference between aircraft and satellite values of $dG_a/d(SST)$ may result, in part, from the gradient of convection with SST being larger than climatology during the experiment (*20*). TOA, top of the atmosphere.

Altitude (mbar)	dG_a/dSST (aircraft) (W m^{-2} K^{-1})	dG_a/dSST (satellite) (W m^{-2} K^{-1})
TOA		6–9‡
69	15.3*	
	14.2†	
191	13.5*	

*Determined with irradiances from the IRBBR. †Determined with radiances from the NFOV. ‡From (*12*).

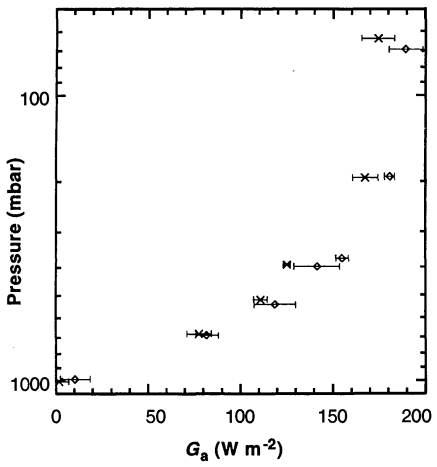

Fig. 4. Vertical profiles of clear sky greenhouse effect east (diamonds) and west (crosses) of the dateline. Bars indicate standard deviations and reflect the change in G_a with SST at each altitude.

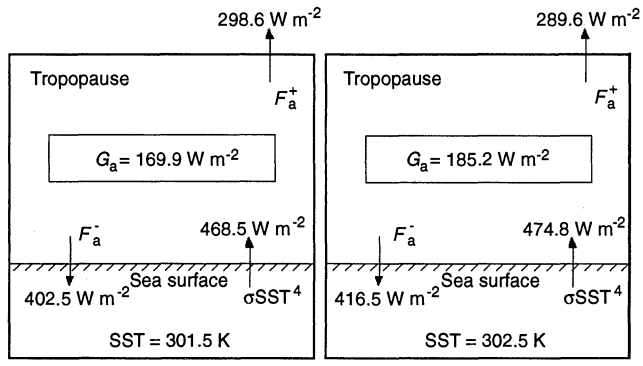

Fig. 5. Summary of the measurements of the clear-sky water vapor greenhouse effect. The values of G_a, F_a^+, and F_a^- are shown schematically for SSTs of 301.5 and 302.5 K at sea level and at 69 mbar (tropopause). G_a increases by 15.3 W m^{-2} K^{-1}, F_a^+ by 6.3 W m^{-2}, and F_a^- by 14 W m^{-2} K^{-1} (*23*), illustrating that the energy absorbed by the clear sky tropospheric water vapor greenhouse effect is radiated back to the surface, thus contributing to its heating.

change of surface emission at 300 K (~6.1 W m^{-2} K^{-1}) and are larger than previously derived satellite values (*9*, *12*, *19*, *20*) as shown in Table 1.

During the time of the experiment, differences (up to 40%) in precipitable water and convective activity were observed between regions east and west of the dateline (*19*). Therefore, the data were divided into two groups to produce tropospheric greenhouse effect profiles in convectively suppressed (east) and convectively active (west) regions. The profiles shown in Fig. 4 were constructed by using P-3 data for the mid- and lower troposphere (400 mbar and below), Learjet data for the upper troposphere (~191 mbar), and ER-2 data for the tropopause (~69 mbar). A comparison of the G_a profiles suggests that the greenhouse absorption is greater in the convectively active region west of the dateline at every level measured by the aircrafts. Our sample in the convectively active region is not large enough to prove this point; however, vertical profiles of atmospheric temperature and humidity measured with dropsondes launched from the learjet in conjunction with the radiometric measurements provide further support for this observation. The greenhouse effect was computed from these soundings with a radiative transfer model (*21*, *22*). Regression of the calculated G_a against SST and satellite indices of convective activity also gives values for G_a that are systematically larger in convective regions. The analysis also shows that the perturbations in G_a by convection at fixed SST are comparable in magnitude with the effect of increasing SST by 2 K. This effect results primarily from local moistening of the atmospheric column by deep convection.

Lubin (*23*) finds $dF_a^-/d(\mathrm{SST}) > 4\sigma(\mathrm{SST})^3$ for surface observations, and our results show $dG_a/d(\mathrm{SST}) > 4\sigma(\mathrm{SST})^3$ for tropopause and tropospheric measurements. Furthermore, by comparison we find $dG_a/d(\mathrm{SST}) \approx d(F_a^-)/d(\mathrm{SST})$, demonstrating that the radiation absorbed as greenhouse effect is radiated back to the surface and contributes to surface heating (Fig. 5). The observed net surface heating due to the water vapor greenhouse effect affects those regions of the tropical oceans that have been shown by general circulation model studies to be key areas for climate change and global warming.

REFERENCES AND NOTES

1. N. E. Graham, *Science* **267**, 666 (1995).
2. P. D. Jones, T. M. Wigley, P. B. Wright, *Nature* **322**, 430 (1986).
3. J. Hansen and S. Lebedeff, *J. Geophys. Res.* **92**, 13345 (1987).
4. J. K. Angell, *Geophys. Res. Lett.* **17**, 1097 (1990).
5. Y. H. Pan and A. H. Oort, *Mon. Weather Rev.* **111**, 1244 (1983).
6. R. E. Newell and B. C. Weare, *Nature* **262**, 40 (1976); *Science* **194**, 1413 (1976).
7. M. Lal and V. Ramanathan, *J. Atmos. Sci.* **41**, 2238 (1984).
8. A. Raval and V. Ramanathan, *Nature* **342**, 758 (1989).
9. G. L. Stephens and T. J. Greenwald, *J. Geophys. Res.* **96**, 15311 (1991).
10. R. Hallberg and A. K. Inamdar, *J. Clim.* **6**, 920 (1992).
11. T. H. VonderHaar, *NASA Refer. Publ.* **1169**, 87 (1986).
12. V. Ramanathan and W. Collins, *Nature* **351**, 27 (1991).
13. F. P. J. Valero, W. J. Y. Gore, L. P. Giver, *Appl. Opt.* **21**, 831 (1982).
14. P. D. Hammer, F. P. J. Valero, S. Kinne, *Mon. Weather Rev.* **119**, 1673 (1991).
15. R. W. Reynolds, *J. Clim.* **1**, 75 (1988).
16. J. D. Spinhirne, W. D. Hart, D. L. Hlavka, *J. Atmos. Sci.* **53**, 1438 (1996).
17. M. D. King *et al.*, *J. Atmos. Oceanogr. Tech.* **13**, 777 (1996).
18. V. Ramanathan *et al.*, *Science* **243**, 57 (1989).
19. Calculations, in which temperature and water vapor profiles obtained with soundings from the research vessel Vickers and climatological summer time profiles above 150 mbar were used, show that the difference between top-of-the-atmosphere and tropopause irradiances is 1.6 W m^{-2} at a fixed 4- to 40-μm bandpass with no change in $dG_a/d(\mathrm{SST})$. The top-of-the atmosphere 4- to 500-μm and 4- to 40-μm irradiances differ by 10 W m^{-2} with no effect in $dG_a/d(\mathrm{SST})$.
20. The satellite data represent a global 5-year record, whereas our data cover 1 month of observations in the central Pacific. We have used the National Center for Atmospheric Research community climate model to check this point. The model reproduces the satellite $dG_a/d(\mathrm{SST})$ very accurately [J. T. Kiehl and B. P. Briegleb, *J. Geophys. Res.* **97**, 10037 (1992)]. However, when the model output is conditionally sampled with the bivariate probability distribution of SST and outgoing longwave radiation corresponding to the domain and time period of our experiment, the model yields $G_a = [147.4 + 13.0(\mathrm{SST} - 300)]$ W m^{-2} at the tropopause. This result is very close to the aircraft values. Because the same model can reproduce both the satellite and aircraft results, depending on how its output is sampled, we conclude that the observed difference may be a consequence of conditions sampled during the observations.
21. C. P. Weaver, W. D. Collins, H. Grassl, *J. Geophys. Res.* **99**, 25891 (1995).
22. The dropsondes released from the Learjet provided reliable data only at pressures higher than 245 mbar. A calculation of G_a at 300 mbar gives $G_a = [134.9 + 13.1(\mathrm{SST} - 300)]$ W m^{-2}.
23. D. Lubin, *Science* **265**, 224 (1994).

24. We thank V. Ramanathan for helpful discussions and critical reading of the manuscript. Supported by NSF grant 9223467. The NASA Radiation Sciences Program facilitated the use of the ER-2 aircraft during the experiment.

30 September 1996; accepted 30 January 1997

Direct Radiative Forcing by Smoke from Biomass Burning

Peter V. Hobbs, Jeffrey S. Reid, Robert A. Kotchenruther, Ronald J. Ferek, Ray Weiss

Airborne measurements in smoke from biomass burning in Brazil have yielded optical parameters that permit an improved assessment of the effects of smoke on Earth's radiation balance. The global-mean direct radiative forcing due to smoke from biomass burning worldwide is estimated to be no more than about −0.3 watt per square meter (cooling), compared with +2.45 watts per square meter (warming) due to anthropogenic greenhouse gases. On regional scales, direct radiative forcing due to smoke can be large and might indirectly affect global climate.

Radiative forcing (*1*) due to increases in long-lived greenhouse gases since preindustrial times is know rather precisely: +2.45 ± 0.37 W m^{-2} (*2*). Direct radiative forcing (DRF) due to increases in anthropogenically derived aerosols, on the other hand, is quite uncertain: −0.5 W m^{-2} is the global average, with an uncertainty of at least a factor of 2 (*2*, *3*). Until the magnitude of radiative forcing due to anthropogenically derived aerosols is known more precisely, the uncertainty in the estimate of the net radiative forcing due to anthropogenic emissions of gases and particles, and therefore predictions of global warming, will remain unacceptably large.

The main contributors to radiative forcing by anthropogenic aerosols are believed to be sulfate particles from fossil fuel combustion and smoke particles from biomass burning. About 80% of all biomass burning occurs in the tropics, and South America accounts for about 30% of all tropical burning (*4*). Penner *et al.* (*5*) estimated the global-mean DRF due to biomass burning to be −0.8 W m^{-2} (*6*). We describe here a comprehensive set of measurements of the optical properties of smoke from biomass burning in Brazil (*7*). We then assess the effects of these measurements on estimates of the global-mean DRF due to smoke from biomass burning using a model similar to that used by Penner *et al.*

To quantify DRF due to aerosols, the magnitudes of four optical properties of the aerosols are required: the mass light-scattering efficiency, the fraction of solar radiation backscattered to space, the single-scattering albedo [that is, the ratio of the light-scattering coefficient (σ_s) to the total extinction

P. V. Hobbs, J. S. Reid, R. A. Kotchenruther, R. J. Ferek, Department of Atmospheric Sciences, University of Washington, Seattle, WA 98195–1640, USA.
R. Weiss, Radiance Research, Seattle, WA 98177, USA.